Site Occupancies, VUV-UV-vis Photoluminescence, and X-ray Radioluminescence of Eu^{2+}-Doped RbBaPO$_4$

Zhou, Rongfu; Ma, Fengkai; Su, Fang; Ou, Yiyi; Qi, Zeming; Zhang, Jianhui; Huang, Yan; Dorenbos, Pieter; Liang, Hongbin

Important note
To cite this publication, please use the final published version (if applicable).
Please check the document version above.

Inorganic Chemistry

Site Occupancies, VUV-UV−vis Photoluminescence, and X-ray Radioluminescence of Eu²⁺-Doped RbBaPO₄

Rongfu Zhou, Fengkai Ma, Fang Su, Yiyi Ou, Zeming Qi, Jianhui Zhang, Yan Huang, Pieter Dorenbos, and Hongbin Liang*

Read Online

ACCESS | Metrics & More | Article Recommendations | Supporting Information

ABSTRACT: RbBaPO₄:Eu²⁺ phosphors have been prepared by a high-temperature solid-state reaction method, and the structure was determined by Rietveld refinement based on powder X-ray diffraction (P-XRD) data. Their VUV-UV−vis photoluminescence properties are systematically investigated with three objectives: (1) based on low-temperature spectra, we clarify the site occupancies of Eu²⁺, and demonstrate that the doublet emission bands at ∼406 and ∼431 nm originate from Eu²⁺ in Ba²⁺ [Eu²⁺(I)] and Rb⁺ [Eu²⁺(II)] sites, respectively; (2) an electron-vibrational interaction (EVI) analysis is conducted to estimate the Huang−Rhys factors, the zero-phonon lines (ZPLs) and the Stokes shifts of Eu²⁺ in Rb⁺ and Ba²⁺ sites; (3) the studies on luminescence decay of Eu²⁺(I) reveal that dipole−dipole interaction is mainly responsible for the energy transfer from Eu²⁺(I) to Eu²⁺(II), and the energy migration between Eu²⁺(I) is weak. Finally, the X-ray excited luminescence (XEL) spectrum indicates that the light yield of the sample RbBa₀.₉₉₅Eu₀.₀₀₅PO₄ is ∼17 700 ph/MeV, showing its potential application in X-ray detecting.
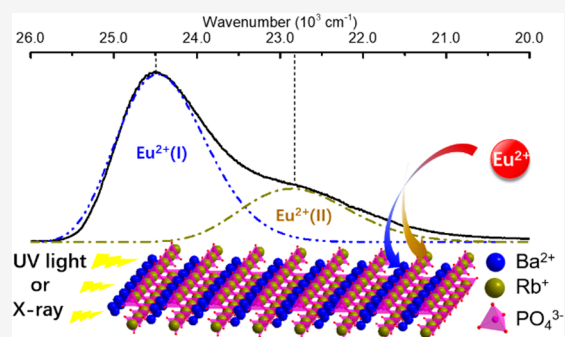
1. INTRODUCTION

Eu²⁺ is one of the lanthanide ions and has 4f⁷ electronic configuration. It shows 5d−4f emission when the lowest 4f⁶5d state is located below the ⁶P_J level, and has been extensively studied for applications in lighting, display, and scintillation detection. BaMgAl₁₀O₁₇:Eu²⁺ has been a suitable blue-emitting phosphor in tricolor lamps for years, BaFCl:Eu²⁺ is the first commercially available rare-earth X-ray phosphor, SrAl₂O₄:Eu²⁺, Dy³⁺ is a long phosphorescent phosphor with high brightness and is widely applied, SrI₂:Eu²⁺ is a scintillator with high light output for detecting ionizing radiation, and Sr[LiAl₃N₄]:Eu²⁺ is considered to be a potential red-emitting phosphor for next-generation high-power phosphor-converted white-light-emitting diodes.[1−4]

The following aspects are essential for the development of novel Eu²⁺-doped luminescent materials. First, the site occupancy of the doping lanthanide ion must be clarified, because it is one of the most crucial factors for the excitation and emission wavelengths of Eu²⁺ in a specific host compound.[5,6] For instance, the excitation peaks of Eu²⁺ in the 10-fold coordinated Sr²⁺ site and 6-fold coordinated Ca²⁺ site of Li₄SrCa(SiO₄)₂ are found at ∼290 and ∼375 nm, respectively.[7] The emission bands at ∼472, ∼445 and ∼406 nm are assigned to Eu²⁺ at Sr(I)O₉, Sr(III)O₈, and Sr(II)O₇ polyhedral sites in Sr₅SiO₄Cl₆, respectively.[8] The blue emission peaking at 471 nm originated from the occupancies of Eu²⁺ in the monovalent cation sites Rb⁺, Na1⁺, and Na2⁺ in RbNa₃(Li₃SiO₄)₄.[9] Eu²⁺ occupies the LuO₆ and K2O₆ polyhedrons in K₃LuSi₂O₇ with deep red emissions.[10] Second, the electron-vibrational interaction (EVI) is another important factor for the luminescence properties of rare earth ions. It has significant influence on the position and the width of the emission band of Eu²⁺.[11−13] Third, the investigations on the energy-transfer dynamics through fluorescence decays are beneficial to understanding the luminescence processes.[14,15]

The compound RbBaPO₄ belongs to ABPO₄ (A is an alkali metal, B is an alkali earth metal) type orthophosphates; it has good thermal and hydrolytic stability and wide band gap.[16−21] On the basis of systematic studies on the VUV-UV−vis photoluminescence and X-ray radioluminescence of Eu²⁺-doped RbBaPO₄, in this paper, we report a potential X-ray phosphor RbBa₀.₉₉₅Eu₀.₀₀₅PO₄ after discussions on the site occupancies, the EVI, and the energy-transfer dynamics in detail.
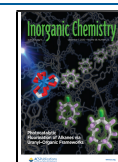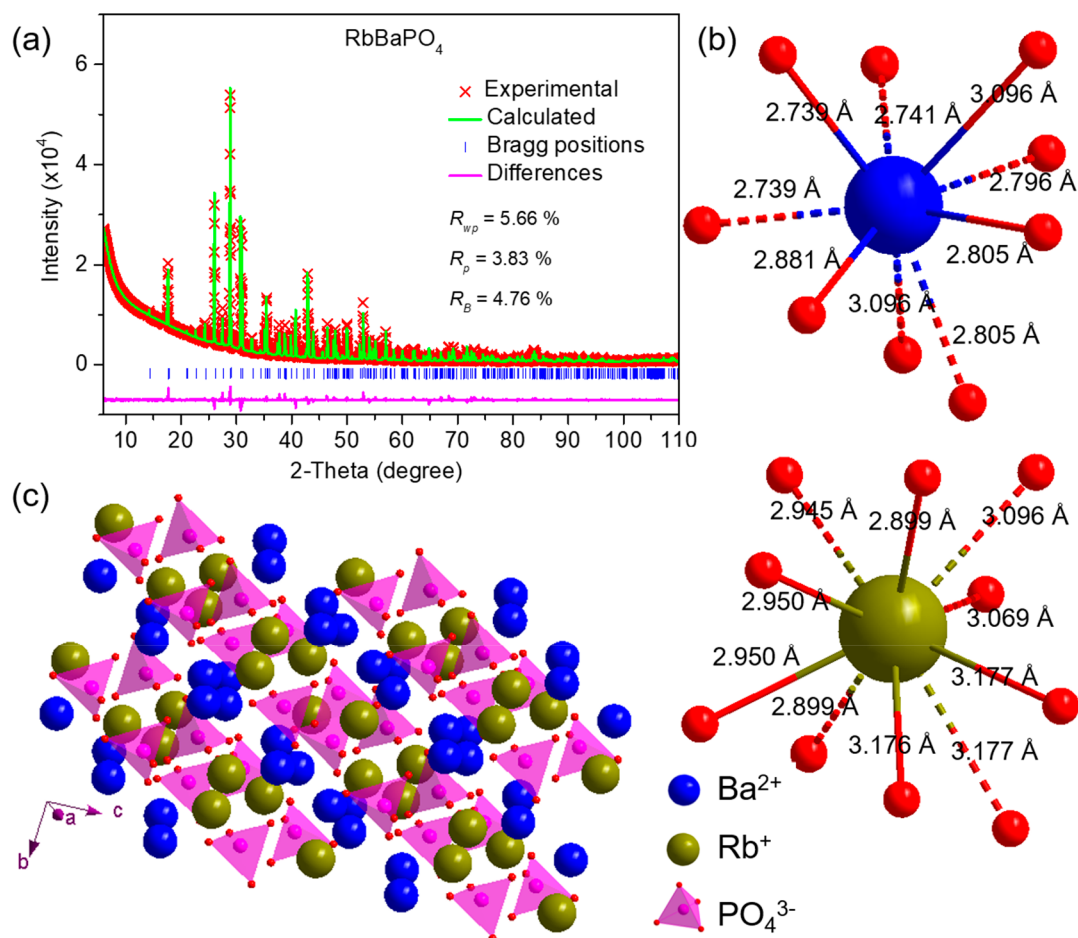
Figure 1. (a) Rietveld refinement of P-XRD data of synthesized RbBaPO$_4$ sample; (b) the coordination environments of Ba^{2+} and Rb$^+$ sites; (c) the 2 × 2 × 2 lattice cell structure of RbBaPO$_4$.

2. EXPERIMENTAL SECTION

2.1. Preparation. The pure host compound and Eu^{2+}-doped RbBaPO$_4$ samples were prepared using a conventional solid-state reaction route at high temperature. The analytic reagents BaCO$_3$, Rb$_2$CO$_3$, (NH$_4$)H$_2$PO$_4$, and 99.99% pure rare-earth oxides Eu$_2$O$_3$ were used as starting materials. The reactants were weighed with nominal formulas RbBa$_{1-x}$Eu$_x$PO$_4$ and ground thoroughly in an agate mortar. The mixtures were moved to alumina crucibles and prefired at 975 K in air atmosphere for 3 h. Eu^{2+}-doped samples were then annealed at 1275 K for 6 h under the CO ambience, which was produced from the incomplete combustion of carbon at high temperature. After cooling down to room temperature (RT), the final products were ground into powders for subsequent analyses.

2.2. Characterizations. The phase purity of the synthetic samples was estimated by powder X-ray diffraction (P-XRD) on a Rigaku D-MAX 2200 VPC X-ray diffractometer of Cu Kα (λ = 1.5418 Å) radiation at 40 kV and 26 mA. The P-XRD data for refinement were collected with the 2θ range from 5 to 110° and a 2θ step of 0.02° on the Bruker D8 advanced X-ray diffractometer with a wavelength of 1.54056 Å Cu Kα radiation at 40 kV and 40 mA. The Rietveld refinement was performed using the *TOPAS Academic* program.[22]

The UV−vis excitation and emission spectra as well as the luminescence decay curves at room temperature (RT) were recorded on an Edinburgh FLS 1000 model spectrometer, which was a combined fluorescence lifetime and steady state, equipped with a cooled housing (−20 °C) photomultiplier PMT-900. The 450 W xenon lamp was used as the excitation source of steady-state excitation and emission spectra. A 150 W nF900 lamp with a pulse width of 1 ns and pulse repetition rate of 40 kHz was used for the measurements of decay curves. The temperature-dependent spectral measurements in

the 77−500 K range were performed by mounting the samples in an Oxford cryostat. The spectral measurements at 15 K were performed by mounting the samples in an Oxford cryostat with a closed cycle liquid helium apparatus and an Edinburgh FLS 920. The emission spectra of RbBa$_{1-x}$Eu$_x$PO$_4$ (x = 0.001, 0.02, and 0.06) samples at 15 K as shown in Figure S1a−c were measured about a half a year later than that of the RbBa$_{0.995}$Eu$_{0.005}$PO$_4$ sample to further confirm the dual-site occupancies of Eu^{2+} in RbBaPO$_4$.

The excitation and emission spectra in the VUV-UV range were recorded on the 4B8 beamline of the Beijing Synchrotron Radiation Facility (BSRF). The sample was pressed into a pill with diameter of about 1 cm and thickness of about 0.2 cm for middle and far-infrared reflectance (IR) spectrum measurement on U4 beamline of National Synchrotron Radiation Laboratory (NSRL). For X-ray excited luminescence spectra measurements of 100 mg pressed pill samples at Delft University of Technology (The Netherlands), an X-ray tube with a tungsten anode operated at 80 kV was used as X-ray source.

3. RESULTS AND DISCUSSION

3.1. P-XRD Patterns and Structure. Based on the P-XRD data of the synthesized RbBaPO$_4$ sample, Figure 1a shows the results of Rietveld refinement which is performed by using *Pnma* structure mode.[20,23] The sample is of pure phase, and as-obtained reliability factors R_{wp}, R_p, and R_B indicate good goodness-of-fit results. The final refined structural parameters are listed in Table S1. The lattice constants a, b, and c and unit-cell volume V of RbBaPO$_4$ are 7.8178(8), 5.7386(4), 10.0586(0), and 451.26(8) Å^3, respectively.
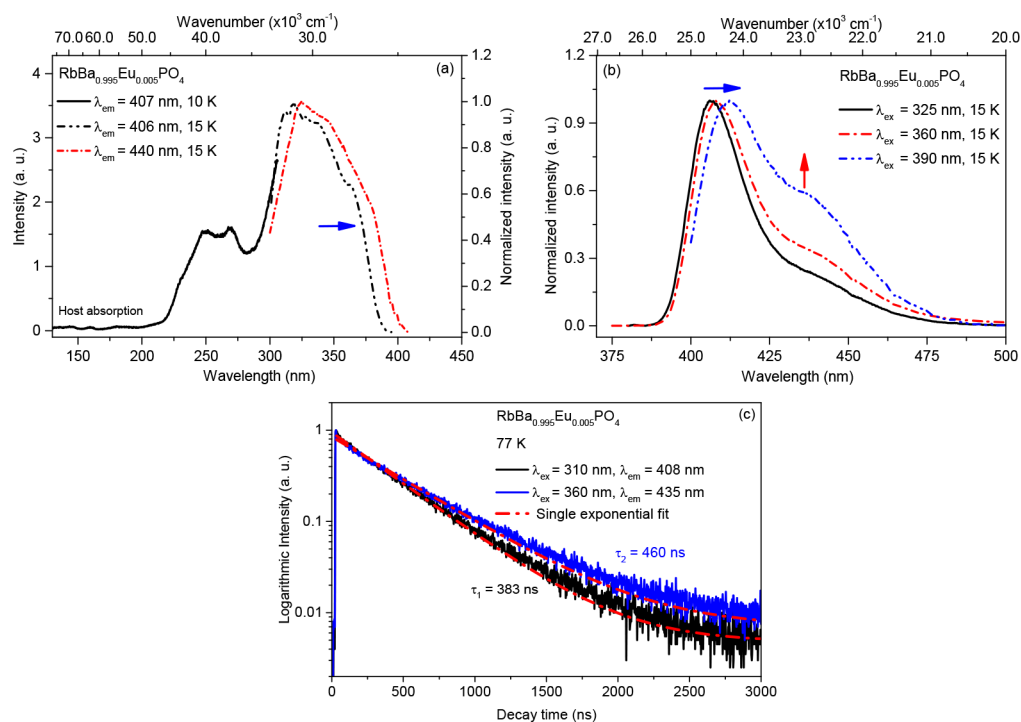
Figure 2. (a) Synchrotron radiation VUV-UV excitation (λ_{em} = 407 nm; 10 K) and the highest-height normalized lab UV−vis excitation (λ_{em} = 406 and 440 nm; 15 K) spectra of RbBa$_{0.995}$Eu$_{0.005}$PO$_4$ sample; (b) the highest-height normalized emission (λ_{ex} = 325, 360, and 390 nm; 15 K) spectra of RbBa$_{0.995}$Eu$_{0.005}$PO$_4$ sample; (c) the decay curves (λ_{ex} = 310 nm, λ_{em} = 408 and λ_{ex} = 360 nm, λ_{em} = 435 nm; 77 K) of RbBa$_{0.995}$Eu$_{0.005}$PO$_4$ sample.

RbBaPO$_4$ has two metal cation sites Ba^{2+} and Rb$^+$. The coordination environments of Ba^{2+} and Rb$^+$ sites are displayed in Figure 1b and the bond lengths of Ba^{2+}−O$^{2−}$ and Rb$^+$−O$^{2−}$ are listed in Table S2. The Ba^{2+} ion is connected with nine O$^{2−}$ ions with low point symmetry C_s, whereas Rb$^+$ is larger than Ba^{2+} and coordinated by ten O$^{2−}$ ligands. The average bond length of Ba^{2+}−O$^{2−}$ is ~2.855 Å, and that of Rb$^+$−O$^{2−}$ is ~3.031 Å. The nearest distance of Rb$^+$−Rb$^+$ (~4.177 Å) is close to that of Ba^{2+}−Ba^{2+} (~4.064 Å). Figure 1c shows the 2 × 2 × 2 lattice cell structure of RbBaPO$_4$ host. The Rb$^+$ ions mainly distribute along the b direction, whereas the Ba^{2+} ions parallelly distribute along the lattice planes the of a and c axes to construct Ba^{2+} layers. The Ba^{2+} layers stack along the b crystal axis. The BaO$_9$, RbO$_{10}$, and PO$_4$ polyhedra form the RbBaPO$_4$ structure.

The P-XRD patterns of RbBa$_{1−x}$Eu$_x$PO$_4$ (x = 0.001−0.08) samples and the refined result of RbBaPO$_4$ are shown in Figure S2. All samples are in agreement with the refined results. This indicates that Eu^{2+} ions are successfully incorporated into RbBaPO$_4$ lattices. The high-quality P-XRD patterns of selected RbBa$_{1−x}$Eu$_x$PO$_4$ (x = 0.02, 0.04 and 0.08) samples and their Rietveld refinement results are shown in Figure S3a−c. The obtained reliability factors R_{wp}, R_p, and R_B indicate a good refined quality. It is demonstrated that RbBa$_{1−x}$Eu$_x$PO$_4$ samples are single purity phase.

3.2. VUV-UV−vis Photoluminescence of RbBa$_{0.995}$Eu$_{0.005}$PO$_4$.
Plots a and b in Figure 2 are the VUV-UV excitation spectrum (λ_{em} = 407 nm) recorded with synchrotron radiation facility at BSRF at 10 K, the highest-height normalized UV−vis excitation (λ_{em} = 406 and 440 nm) and the emission (λ_{ex} = 325, 360, and 390 nm) spectra collected by FLS 920 spectrometer of RbBa$_{0.995}$Eu$_{0.005}$PO$_4$ sample at 15 K. It shows that the excitation intensity below

~200 nm in Figure 2a is very weak. For host compounds with similar compositions to RbBaPO$_4$, we found in previous work the host exciton peaks at ~7.61 eV in NaCaPO$_4$ and ~7.65 eV in KSrPO$_4$, respectively.[17,20] The weak excitonic absorption in the current case may relate to the low energy-transfer probability from host to doping Eu^{2+} ions, the delocalization of Eu^{2+} 5d electron into the conduction band when the high-lying 5d excited states are higher than the conduction band minimum,[24] and/or other unknown reasons. To determine the exciton peak location of RbBaPO$_4$, the VUV excitation spectra of two samples Rb$_{1.02}$Ba$_{0.96}$Gd$_{0.02}$PO$_4$ and Rb$_{1.003}$Ba$_{0.994}$Ce$_{0.003}$PO$_4$ were recorded at 10 K and shown in Figures S4 and S5, respectively. The host exciton peak (E_{ex}) is found to be ~7.37 eV (168 nm) in Figure S4 and ~7.43 eV (167 nm) in Figure S5. The mean value 7.40 ± 0.03 eV of RbBaPO$_4$ found from Figures S4 and S5 is compatible with the values of NaCaPO$_4$ and KSrPO$_4$.[17,20] So the band gap of RbBaPO$_4$ is estimated to be 7.84 eV after extra adding exciton binding energy ($0.008E_{ex}^2$ = 0.44 eV) to E_{ex} (7.40 eV).

The strong excitation bands beyond 220 nm result from 4f−5d transitions of Eu^{2+}. The profiles of the two excitation curves in the 300−410 nm range are somewhat different, by monitoring emissions at 406 and 440 nm, respectively. The excitation band of 440 nm emission slightly shifts to the long-wavelength side in comparison with that of 406 nm emission. We suspect that these observations relate to different site occupancies of Eu^{2+} in the RbBa$_{0.995}$Eu$_{0.005}$PO$_4$ sample and will discuss this issue below.

Upon 325 nm excitation, we record the main emission peak at about 406 nm and a weak shoulder band at about 431 nm in Figure 2b. When we move the excitation wavelength to 360 and 390 nm, the shoulder emission band gradually becomes more pronounced and the main emission peak slightly shifts to
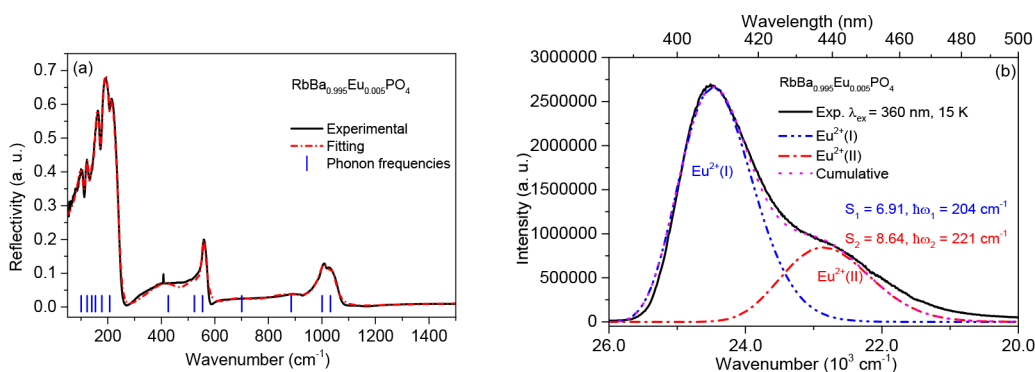
Figure 3. (a) Experimental and fitted synchrotron radiation infrared reflectance spectrum of $RbBa_{0.995}Eu_{0.005}PO_4$ at RT; (b) the emission spectrum (λ_{ex} = 360 nm; 15 K) and corresponding electron-vibrational interaction (EVI) analysis.

about 407 and 410 nm. The phenomenon can be seen not only in this $RbBa_{0.995}Eu_{0.005}PO_4$ sample, but also in other samples. As shown in Figure S1a−c, similar results were recorded in samples $RbBa_{1−x}Eu_xPO_4$ (x = 0.001, 0.02, and 0.06), although these three samples were stored for about half a year before the measurement. The main peak shifts to the long-wavelength direction and the shoulder band is more conspicuous under 390 nm excitation in comparison with that under 325 and 360 nm excitation. These observations are somewhat different from those in references, in which only a broad asymmetric band was seen, but no shoulder band was found in the emission spectra.[16,19] Besides, the emission peaks were reported to shift to longer wavelengths with the increase in Eu^{2+} concentrations, and the red shift of the emission band was explained by the change in the crystal field around Eu^{2+}. Because no impurity phase was detected in these samples as mentioned in section 3.1, we think that the dual-site occupancies of Eu^{2+} ions may be the main reason for the evolution of the emission profile under different excitation wavelengths in this paper. Because Ba^{2+} and Eu^{2+} ions have similar ionic radii and the same valence states, the Ba^{2+} site should be one of the two sites that Eu^{2+} occupies.

The emission energy of Eu^{2+} at the Ba^{2+} site of $RbBaPO_4$ can be predicted using the equation $E(Eu^{2+})$ = (0.64 ± 0.02) $E(Ce^{3+}) + (0.53 \pm 0.06)$ eV.[25] Ce^{3+} ions have been reported to occupy Ba^{2+} sites in $RbBaPO_4$.[18] In Figure S5, the doublet $5d_1$-$^2F_{5/2,7/2}$ emissions of Ce^{3+} in $Rb_{1.003}Ba_{0.994}Ce_{0.003}PO_4$ are approximately observed at 3.83 and 3.58 eV, respectively. Using above equation, the emission energy of Eu^{2+} at the Ba^{2+} site of $RbBaPO_4$ is predicted to be at 2.98 ± 0.14 eV ($\sim$416 nm). This position is closer to the main peak at about 406 nm and shows more differences from the shoulder band at about 431 nm. It seems to imply that the main peak at 406 nm is from the emission of Eu^{2+} at the Ba^{2+} site and that the shoulder band is the emission of Eu^{2+} at another type of site. However, because of the error margin of approximately 0.2 eV of the prediction, we do not merely use this prediction as an unambiguous argument to assign the site occupancies of Eu^{2+} ions.

The site nature can be further understood by the comparison of the emission of Eu^{2+} in isomorphic host compounds $KSrPO_4$, $KBaPO_4$, and $RbBaPO_4$.[20,26,27] These compounds crystallize in an orthorhombic structure with the space group *Pnma*, and have a single 9-fold coordinated Sr^{2+} or Ba^{2+} site with C_s point symmetry. Referring to the data in Table S3, the emission peak of Eu^{2+} at the Ba^{2+} site of $KBaPO_4$ has been observed at 419 ± 2 nm, and that at the Sr^{2+} site of $KSrPO_4$ was found at 423 ± 1 nm.[19,20,26] Because the BaO_9 polyhedron is larger than that of SrO_9, the crystal field splitting (CFS) energy of the Eu^{2+} 5d orbital at the Ba^{2+} site is likely to be smaller than that at the Sr^{2+} site. As a result, the emission wavelength of Eu^{2+} at the Ba^{2+} site of $KBaPO_4$ (419 ± 2 nm) is expected be slightly shorter than that at the Sr^{2+} site of $KSrPO_4$ (423 ± 1 nm). Similarly, it is expected that the emission peak of Eu^{2+} at the Ba^{2+} site of isomorphic $RbBa_{0.995}Eu_{0.005}PO_4$ locates at shorter wavelength ($<423 \pm 1$ nm). So the main peak of about 406 nm is attributed to the emission of Eu^{2+} at Ba^{2+} site of $RbBa_{0.995}Eu_{0.005}PO_4$ (marked as $Eu^{2+}(I)$), and the shoulder band of about 440 nm is ascribed to the emission of Eu^{2+} at another type of site (labeled as $Eu^{2+}(II)$). The $Eu^{2+}(II)$ is most likely Eu^{2+} in the Rb^+ site in consideration of the structure of $RbBaPO_4$.

To evaluate the positions of the main and shoulder bands, we fitted the emission curves with a sum of two Gaussian functions (Figure S6). Under 325 nm excitation, two peaks are at $\sim24.6 \times 10^3$ cm^{-1} (406 nm) and $\sim23.2 \times 10^3$ cm^{-1} (431 nm). They show a slight red shift when excited at 360 nm. Upon 390 nm excitation, the two peaks shift to $\sim24.4 \times 10^3$ cm^{-1} (410 nm) and $\sim23.1 \times 10^3$ cm^{-1} (433 nm). The longer wavelength is more likely to excite $Eu^{2+}(II)$ ions, so the relative intensity of $Eu^{2+}(II)$ emission becomes gradually stronger under 325, 360, and 390 nm excitation. Two factors, the increasing emission intensity of $Eu^{2+}(II)$ and the conjoint influences of $Eu^{2+}(I)$ and $Eu^{2+}(II)$ emissions, make both bands appear to shift toward longer wavelengths in fitting results. The increase in $Eu^{2+}(II)$ emission draws the main emission peak toward the long wavelength direction, and the red shift of the main peak, in turn, makes the shoulder band appear at the longer wavelength side.

Finally, we recorded two decay curves (λ_{ex} = 310 nm, λ_{em} = 408; λ_{ex} = 360 nm, λ_{em} = 435) of $Eu^{2+}(I)$ and $Eu^{2+}(II)$ in $RbBa_{0.995}Eu_{0.005}PO_4$ at 77 K that are displayed in Figure 2c. Decay curves show an exponential characteristic. Each decay curve was fitted with single exponential decay functions to obtain the lifetimes τ_1 = 383 ns and τ_2 = 460 ns for $Eu^{2+}(I)$ and $Eu^{2+}(II)$, respectively. They are in the range of lifetimes reported for other Eu^{2+}-doped materials with similar emission wavelength, such as $BaMgSiO_4$:0.007 Eu^{2+} (420 nm, $\sim$324 ns),[28] $SrAl_3BO_7$:0.03 Eu^{2+} (410 nm, $\sim$430 ns),[29] and $K_{0.2}Rb_{0.8}BaPO_4$:0.03 Eu^{2+} (424 nm, $\sim$484 ns).[19] The ratio τ_1/τ_2 ($\sim$0.83) is close to the ratio $\frac{\lambda_1^3}{\lambda_2^3}$ ($= \frac{406^3}{431^3} = 0.84$), because the radiative decay time is proportional to the third power of the average emission wavelength in a given host.[30]

3.3. Electron-Vibrational Interaction and Temperature-Dependent Luminescence of Eu^{2+} in $RbBa_{0.995}Eu_{0.005}PO_4$.

The Eu^{2+} emission band is formed by a series of electron-vibrational transition lines that have been broadened and smoothed by lattice dispersion. The band shape of Eu^{2+} can be described by the Pekarian-type spectral distribution which can be simplified to eqs 1 and 2 at low temperature ($kT \leq \hbar\omega$).[31] Because the doping content is low ($x = 0.005$) in the case of Figure 3, we neglect the interactions of the 5d excited state and 4f ground state between $Eu^{2+}(I)$ and $Eu^{2+}(II)$ systems herein and roughly regard the total Eu^{2+} emission shape as the sum of the two independent $Eu^{2+}(I)$ and $Eu^{2+}(II)$ emission shapes as expressed in eq 3.

$$I = \frac{e^{-S}S^P}{P!}\left(1 + S^2\frac{e^{-\hbar\omega/kT}}{P+1}\right) \tag{1}$$

$$P = \frac{E_0 - E}{\hbar\omega} \tag{2}$$

$$I_{total} = A_1\frac{e^{-S_1}S_1^{P_1}}{P_1!}\left(1 + S_1^2\frac{e^{-\hbar\omega 1/kT}}{P_1+1}\right)$$
$$+ A_2\frac{e^{-S_2}S_2^{P_2}}{P_2!}\left(1 + S_2^2\frac{e^{-\hbar\omega 2/kT}}{P_2+1}\right) \tag{3}$$

Where A_1 and A_2 are the emission ratios of $Eu^{2+}(I)$ and $Eu^{2+}(II)$, S_1 and S_2 are the Huang−Rhys factors, $\hbar\omega_1$ and $\hbar\omega_2$ the effective phonon energies, and P_1 and P_2 are the number of effective phonons coupled with $Eu^{2+}(I)$ and $Eu^{2+}(II)$ emissions, k is the Boltzmann constant (6.950×10^{-1} (cm K)$^{-1}$), and T is temperature (15 K).

To estimate the possible effective phonon energies, we measured the middle-far IR spectrum of $RbBa_{0.995}Eu_{0.005}PO_4$ in wavenumber 50−1500 cm^{-1} range at RT using synchrotron radiation facility at NSRL as shown in Figure 3a. The experimental curve is fitted with a model for the complex dielectric function consisting of Lorentz oscillators.

$$\varepsilon(\omega) = \varepsilon_\infty + \sum_k \frac{\omega_{p,k}^2}{\omega_{0,k}^2 - \omega^2 - k\gamma_k\omega} \tag{4}$$

Where ε_∞ is the real part of the complex dielectric function at high frequency; $\omega_{p,k}$, $\omega_{0,k}$, and γ_k are the plasma frequency, phonon frequency, and damping factor of the kth oscillator, respectively. The fitting curve is shown in Figure 3a and fitting parameters are listed in Table S4, which provide the initial referred $\hbar\omega_1$ and $\hbar\omega_2$ values for the following fitting procedure of electron-vibrational interaction (EVI) analysis of Eu^{2+} emissions in $RbBa_{0.995}Eu_{0.005}PO_4$.

We select the emission spectrum under 360 nm excitation for the EVI analysis and show the fitting results in Figure 3b. The simulated parameters of EVI analysis of $RbBa_{0.995}Eu_{0.005}PO_4$ sample are listed in Table 1. The coincidence of fitted and experimental curves indicates a good simulation quality. The fitted emission peaks of $Eu^{2+}(I)$ and $Eu^{2+}(II)$ are approximately located at 24.4×10^3 and 22.8×10^3 cm^{-1}, which are near the Gaussian fitting results ($\sim 24.6 \times 10^3$ and $\sim 23.2 \times 10^3$ cm^{-1}, respectively). As a result, the energies of zero-phonon lines (ZPLs) of $Eu^{2+}(I)$ and $Eu^{2+}(II)$ are estimated to be 25.8×10^3 cm^{-1} (388 nm) and 24.7×10^3 cm^{-1} (405 nm), respectively. The ZPL energy of $Eu^{2+}(I)$ is close to the location of the intersection (25.6×10^3 cm^{-1}, 390

Table 1. Simulated Parameters via EVI Analysis in $RbBa_{0.995}Eu_{0.005}PO_4$ Sample

parameters	values
A_1	1.74×10^7
S_1	6.91
$\hbar\omega_1$ (cm^{-1})	204
$E_0(1)$ (cm^{-1})	25.8×10^3
A_2	6.95×10^6
S_2	8.64
$\hbar\omega_2$ (cm^{-1})	221
$E_0(2)$ (cm^{-1})	24.7×10^3

nm) between the normalized excitation spectrum of 406 nm emission and normalized emission spectrum at 325 nm excitation.[13] The effective phonon energies of $Eu^{2+}(I)$ and $Eu^{2+}(II)$ are estimated to be 204 and 221 cm^{-1}, which are close to the value 207.28 cm^{-1} in Table S4. Hence the Stokes shift values ΔS for $Eu^{2+}(I)$ and $Eu^{2+}(II)$ are calculated to be 2.62×10^3 and 3.60×10^3 cm^{-1} according to $\Delta S = (2S - 1)\hbar\omega$, respectively.

The temperature-dependent emission map ($\lambda_{ex} = 310$ nm) of the $RbBa_{0.995}Eu_{0.005}PO_4$ sample is shown in Figure 4a. With increasing temperature, the intensity of the Eu^{2+} emission decreases gradually. To analyze the influence of temperature on the emission shape of Eu^{2+} in the two sites, the emission spectra of 77 and 500 K are selected to be normalized and shown in Figure 4b. With raising temperature, the emission band broadens to the larger wavenumber side. The observation may relate to the different thermal-quenching and thermal-broadening characteristics of two luminescence centers. As a rough estimation, each emission spectrum is fitted by a sum of two Gaussian functions. When temperature increases from 77 to 500 K, the integrated intensity of $Eu^{2+}(I)$ decreases about 35% and that of $Eu^{2+}(II)$ about 44%, but the value of the full width at half-maximum (fwhm) of $Eu^{2+}(I)$ increases approximately 58% (from $\sim 1.35 \times 10^3$ to $\sim 2.1 \times 10^3$ cm^{-1}) and that of $Eu^{2+}(II)$ approximately 47% (from $\sim 1.83 \times 10^3$ to $\sim 2.69 \times 10^3$ cm^{-1}).

3.4. Concentration-Dependent Luminescence Spectra and Energy Transfer Dynamics of $RbBa_{1-x}Eu_xPO_4$ Samples.

To investigate the effect of concentration on $Eu^{2+}(I)$ and $Eu^{2+}(II)$ emission, we collected the emission spectra of $RbBa_{1-x}Eu_xPO_4$ with different doping concentrations ($x = 0.001−0.08$) under 310 nm excitation at RT. Figure 5a shows normalized emission spectra of these samples in terms of the integral intensity of the emission bands. The shoulder band at long wavelength hand lifts gradually with increasing concentration. Meantime, the main emission peak shifts gradually from 406 to 415 nm. These tendencies become more obvious when the doping concentration (x) is above 0.04. According to emission spectra of $RbBa_{1-x}Eu_xPO_4$ in Figure S7, we estimated the total integral area in 380−490 nm range, read the main peak height and the height at 431 nm, and plotted them as a function of doping concentration (x value) in Figure 5b. Herein, the main peak height and the height at 431 nm are regarded as rough indicators of emission intensities of $Eu^{2+}(I)$ and $Eu^{2+}(II)$, respectively. The main peak height increases at first, and reaches a maximum when $x = 0.03$, then decreases with increasing doping concentrations. In contrast, the height at 431 nm always increase with increasing x value except for the point of $x = 0.04$. As a whole, the integral intensity of Eu^{2+} clearly increases with increasing content until
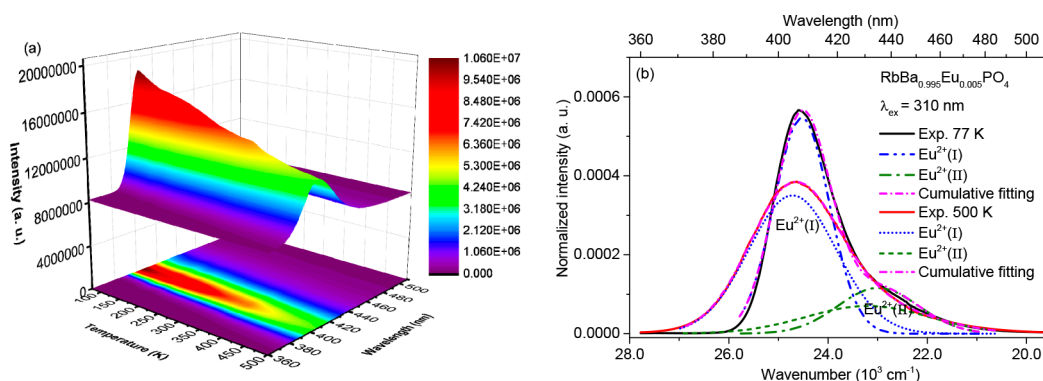
Figure 4. (a) Temperature-dependent emission map (λ_{ex} = 310 nm) of RbBa$_{0.995}$Eu$_{0.005}$PO$_4$ sample; (b) the normalized emission spectra (λ_{ex} = 310 nm) of RbBa$_{0.995}$Eu$_{0.005}$PO$_4$ sample at 77 and 500 K, and corresponding Gaussian fitting results of emission spectra.

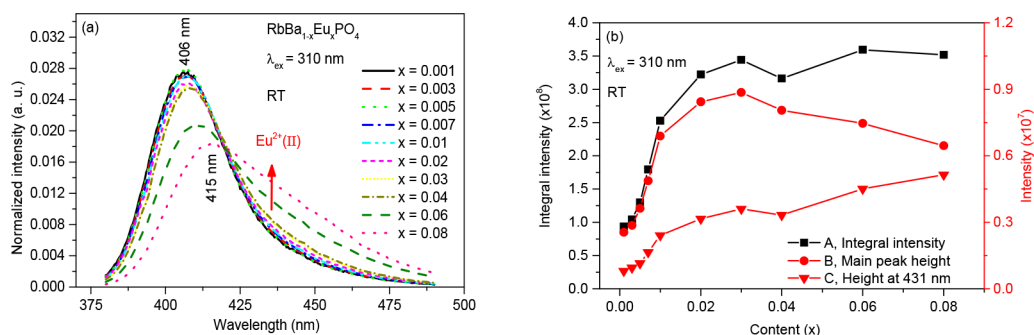**Figure 5.** (a) Normalized emission (λ_{ex} = 310 nm) spectra of RbBa$_{1-x}$Eu$_x$PO$_4$ (x = 0.001−0.08) samples at RT; (b) the dependencies of total integral area in 380−490 nm range (curve A), main peak height (curve B), and the height at 431 nm (curve C) on doping concentrations (x values) in RbBa$_{1-x}$Eu$_x$PO$_4$.
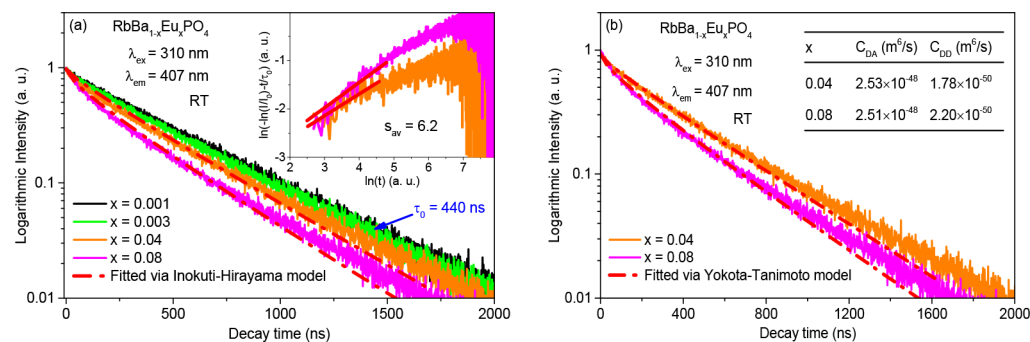

Figure 6. (a) Decay curves (λ_{ex} = 310 nm, λ_{em} = 407 nm) of RbBa$_{1-x}$Eu$_x$PO$_4$ (x = 0.001−0.08) samples at RT and fitting curves via Inokuti−Hirayama model (eq 5), the inset shows linear fitting results with eq 7; (b) the decay curves (λ_{ex} = 310 nm, λ_{em} = 407 nm) of RbBa$_{1-x}$Eu$_x$PO$_4$ (x = 0.04 and 0.08) samples at RT and fitting curves via Yokota−Tanimoto model (eqs 8 and 9).

x = 0.03, and then keeps almost invariable except for the deviation point with x = 0.04. The observations may relate to the factors such as site occupancies, energy transfer between Eu^{2+}(I) and Eu^{2+}(II), and crystal field splitting at different doping levels in following discussions.

At first, when the doping concentration is very low (x = 0.001), Eu^{2+} mainly occupies the Ba^{2+} site and Eu^{2+}(I) emission is dominant. Eu^{2+}(I) emission intensity regularly increases until x = 0.03 due to the increase of population of Eu^{2+} in Ba^{2+} sites. The increase in energy-transfer rates of Eu^{2+}(I) → Eu^{2+}(I) and Eu^{2+}(I) → Eu^{2+}(II) then results in the quenching of Eu^{2+}(I) emission when x > 0.03, and the main peak height decreases. The intensity of Eu^{2+}(II) emission gradually increases, which is ascribed to the contribution of

energy transfer from Eu^{2+}(I) to Eu^{2+}(II) and the increase in Eu^{2+}(II) population with the increase of doping concentration.

The crystal field effect on Eu^{2+} in RbBaPO$_4$ has been regarded as the main reason for the red shift of whole emission band.[16,19] This can be interpreted because the ionic radii increase with the relative order Eu^{2+} < Ba^{2+} < Rb$^+$ in the case of 9- or 10-fold coordination surroundings.[32] With the increase in doping concentration, the Eu^{2+}−O^{2-} bond distance is expected to be somewhat shortened, and the 5d electron of Eu^{2+} experiences a larger crystal field strength. The possible changes in the crystal field around Eu^{2+} are responsible for this shift as reported in BaMg$_2$Si$_2$O$_7$, Ba(PO$_3$)$_2$, K$_2$BaCa(PO$_4$)$_2$, and so on.[15,33,34] When we assume that the energies of the 5d centroid and the Stokes shift are relatively invariant, the 5d−4f emissions of Eu^{2+}(I) and Eu^{2+}(II) shift to the long wavelength

side because of the increase in 5d crystal field splitting of $Eu^{2+}(I)$ and $Eu^{2+}(II)$, respectively. In addition, the increase in the $Eu^{2+}(II)$ component and the decrease in $Eu^{2+}(I)$ also provide a contribution to this red shift.

Further, the energy-transfer dynamics is studied on the basis of decay curves. Figure 6a shows the decay curves (λ_{ex} = 310 nm, λ_{em} = 407 nm) of $RbBa_{1-x}Eu_xPO_4$ (x = 0.001−0.08) samples at RT. At low doping contents with x = 0.001 and 0.003, the decay curves are close to single exponential. When x increases, the decay curves deviate gradually from that of the low doping cases. Several mechanisms of energy transfer such as multipolar and even exchange interactions could make contributions to the deviation. Since the exchange interaction only occurs in very short distances (∼5 Å), the multipolar interactions are expected to be dominated for our samples with the doping content below 10%. To estimate the type of multipolar interaction of energy transfer, we consider only the energy transfer from $Eu^{2+}(I)$ to $Eu^{2+}(II)$ without energy migration between donor $Eu^{2+}(I)$ ions first and simulate the decay curves of donor $Eu^{2+}(I)$ with the Inokuti−Hirayama model as follows:[35]

$$I(t) = I(0)\exp\left[\frac{-t}{\tau_0} + Q(t)^{3/s}\right] \tag{5}$$

$$Q = -\frac{4\pi}{3}n_a\Gamma\left(1 - \frac{3}{s}\right)(C_{DA}^{(s)})^{3/s} \tag{6}$$

$$\ln\left(-\ln\left(\frac{I(t)}{I(0)}\right) - \frac{t}{\tau_0}\right) = \ln(-Q) + \frac{3}{S}\ln(t) \tag{7}$$

Where $I(t)$ is emission intensity of Eu^{2+} at time t and $I(0)$ is the emission intensity at t = 0; n_a is the concentration (m^{-3}) of $Eu^{2+}(II)$ at the Rb^+ site, its initial value is estimated by the doping concentration (0.04 or 0.08) before the simulation procedure; C_{DA}^s is the energy-transfer microparameter, which has a relation of energy-transfer probability. $\Gamma(1-3/s)$ is the gamma function and s parameter depends on the type of electric-multipolar interaction. The s values are 6, 8, and 10 for the dipole−dipole, dipole−quadrupole, and quadrupole−quadrupole interactions, respectively. We mathematically make a transformation and plot the $\ln(-\ln(I(t)/I(0) - t/\tau_0))$ as a function of $\ln(t)$ as shown in the inset of Figure 6a. The s value is obtained by the slope $3/s$ from a linear fitting to decay curves with eq 7. The average s value 6.2 is close to 6, implying that the dominant mechanism of Eu^{2+} in $RbBaPO_4$ compound is the dipole−dipole interaction. The result is consistent with the knowledge that Eu^{2+} involves Laporte allowed transitions, and the nonradiative energy transfer between $Eu^{2+}(I)$ and $Eu^{2+}(II)$ would be mainly dipole−dipole mechanism. It is also in agreement with the reported result on the basis of emission spectra.[16] The decay curves are simulated with eq 5. The fitting quality R_{adj}^2 is all more than 0.99. Table S5 lists other fitting parameters of simulation via this model.

In addition, the simulation with the slow energy diffusion model of Yokota−Tanimoto (eq 8 and 9) is applied to verify the energy transfer from $Eu^{2+}(I)$ to $Eu^{2+}(II)$ and possible energy migration between $Eu^{2+}(I)$.[36,37]

$$I(t) = I(0)\exp\left(\frac{-t}{\tau_0}\right)$$
$$\exp\left(Qt^{3/s}\left(\frac{1 + 10.87x + 15.50x^2}{1 + 8.743x}\right)^{3/4}\right) \tag{8}$$

$$x = DC_{DA}^{-1/3}t^{2/3} \tag{9}$$

$$D = 0.5(4\pi n_d/3)^{4/3}C_{DD} \tag{10}$$

Where $I(t)$ is emission intensity of Eu^{2+} at time t and $I(0)$ is the emission intensity when t = 0, n_a is the acceptor concentration (m^{-3}), which is the concentration of $Eu^{2+}(II)$ in our case, and n_d is concentration (m^{-3}) of donors $Eu^{2+}(I)$; their initial values are estimated by the doping concentration (0.04 or 0.08) and emission ratio of $Eu^{2+}(I)$ to $Eu^{2+}(II)$ as mentioned in Section 3.3. C_{DA} is the energy-transfer microparameter, Q is also expressed as eq 6, C_{DD} is energy migration microparameter, x contains the variable t and is expressed in eq 9, D is diffusion parameter; τ_0 is the lifetime of $Eu^{2+}(I)$ in the situation of no $Eu^{2+}(II)$ acceptors around and set to be τ_{av} = 440 ns from the decay curves of x = 0.001 and 0.003. This model is valid in the limit of weak diffusion between donors ($C_{DD} \ll C_{DA}$). When the s parameter is close to 6, the best agreement of fitted curves with experimental data has been achieved as shown in Figure 6b. It indicates that the mechanism of energy transfer is mainly dipole−dipole interaction. The fitting parameters are summarized in Table S5. The average C_{DA} parameter is about 2.52×10^{-48} m s^{-1}, and the average C_{DD} parameter is about 1.99×10^{-50} m s^{-1}, which satisfies the rule of the Yokota−Tanimoto model. Because the diffusion parameter D is not zero and becomes larger at higher doping content, energy migration between $Eu^{2+}(I)$ also takes part in the process of $Eu^{2+}(I) \rightarrow Eu^{2+}(II)$ energy transfer. But the energy migration between $Eu^{2+}(I)$ is weak in comparison with $Eu^{2+}(I) \rightarrow Eu^{2+}(II)$ energy transfer. Therefore, the decay of $Eu^{2+}(I)$ is mainly caused by energy transfer from $Eu^{2+}(I)$ to $Eu^{2+}(II)$ with the mechanism of dominant dipole−dipole interaction. When energy-transfer probability shows the same rate as the decay rate ($1/\tau_0$) of isolated $Eu^{2+}(I)$, the critical distance R_c is calculated to be about 11 Å.

3.5. X-ray Radioluminescence of $RbBa_{0.995}Eu_{0.005}PO_4$. Figure 7 shows the emission spectra of the $RbBa_{0.995}Eu_{0.005}PO_4$ sample and crystal BaF_2 under X-ray excitation at RT. The crystal BaF_2 is measured as a reference, and its absolute scintillation light yields is measured to be ∼10 000 ph/MeV (photons emitted per MeV of absorbed X-ray energy). The emission band maxima at 226 and 310 nm originate from the core valence luminescence and self-trapped-exciton emission.[38] The asymmetric emission band in the $RbBa_{0.995}Eu_{0.005}PO_4$ sample is from $Eu^{2+}(I)$ and $Eu^{2+}(II)$ emissions. The X-ray excited emission spectrum of $RbBa_{0.995}Eu_{0.005}PO_4$ sample is in line with that under VUV-UV excitation. Based on the calculated ratio of integrated intensity to that of BaF_2, the estimated light yield (η) for $RbBa_{0.995}Eu_{0.005}PO_4$ is 17 700 ± 1800 ph/MeV, showing its potential application in X-ray detecting.

4. CONCLUSIONS

In summary, we prepared the compound $RbBaPO_4$ doped with different concentrations of Eu^{2+} ions, the Rietveld refinement
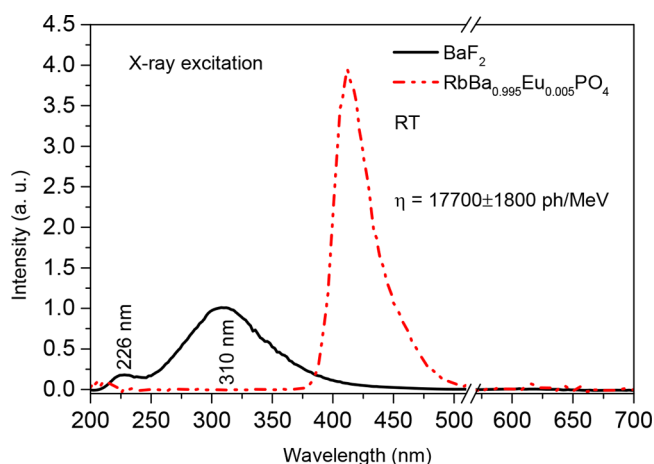
Figure 7. X-ray excited emission spectra of $RbBa_{0.995}Eu_{0.005}PO_4$ sample and crystal BaF_2 at RT.

of P-XRD data confirms that two types of polyhedrons for metal ions occur in the host compound. The RbO_{10} and BaO_9 polyhedrons are with same C_s point symmetry. By using the structural data and the semiempirical formulas, we assign the doublet emission bands of Eu^{2+} ions with the maxima at ~406 and ~431 nm to arise from Eu^{2+} in Ba^{2+} and Rb^+ sites, respectively. The EVI analysis and the temperature-dependent luminescence further corroborate this assignment. Besides, the Huang−Rhys factors, the ZPLs, and the Stokes shifts of Eu^{2+} in Ba^{2+} and Rb^+ sites are estimated by EVI analysis. The energy-transfer dynamics are studied by the measurements on the emission decays of donor Eu^{2+} in the Ba^{2+} site and simulated with the Inokuti−Hirayama model and Yokota−Tanimoto model. The results show that the dominant mechanism of energy transfer is electric dipole−dipole interaction. The light yield value $17\,700 \pm 1800$ ph/MeV of $RbBa_{0.995}Eu_{0.005}PO_4$ estimated from the X-ray excited spectrum indicates the possible application of this phosphor in X-ray detection after further optimization.

ASSOCIATED CONTENT

Supporting Information

The Supporting Information is available free of charge at https://pubs.acs.org/doi/10.1021/acs.inorgchem.0c02714.

P-XRD patterns and Rietveld refinement of P-XRD data of $RbBa_{1−x}Eu_xPO_4$ samples, refined structural parameters of $RbBaPO_4$ sample, fitting parameters for the synchrotron radiation middle-far IR spectrum of $RbBa_{0.995}Eu_{0.005}PO_4$ via the complex dielectric function, fitting parameters of energy-transfer dynamics via two models, highest-height normalized emission spectra (15 K) of $RbBa_{1−x}Eu_xPO_4$ under different excitation wavelengths, VUV-UV excitation and emission spectra (10 K) of $Rb_{1.02}Ba_{0.96}Gd_{0.02}PO_4$, and $Rb_{1.003}Ba_{0.994}Ce_{0.003}PO_4$ samples, highest-height normalized emission spectra of $RbBa_{0.995}Eu_{0.005}PO_4$ sample and corresponding Gaussian fitting results, Emission spectra of $RbBa_{1−x}Eu_xPO_4$ samples. (PDF)

AUTHOR INFORMATION

Corresponding Author

Hongbin Liang − *MOE Key Laboratory of Bioinorganic and Synthetic Chemistry, KLGHEI of Environment and Energy Chemistry, School of Chemistry, Sun Yat-Sen University, Guangzhou 510275, P. R. China;* orcid.org/0000-0002-3972-2049; Email: cesbin@mail.sysu.edu.cn

Authors

Rongfu Zhou − *MOE Key Laboratory of Bioinorganic and Synthetic Chemistry, KLGHEI of Environment and Energy Chemistry, School of Chemistry, Sun Yat-Sen University, Guangzhou 510275, P. R. China*

Fengkai Ma − *MOE Key Laboratory of Bioinorganic and Synthetic Chemistry, KLGHEI of Environment and Energy Chemistry, School of Chemistry, Sun Yat-Sen University, Guangzhou 510275, P. R. China*

Fang Su − *MOE Key Laboratory of Bioinorganic and Synthetic Chemistry, KLGHEI of Environment and Energy Chemistry, School of Chemistry, Sun Yat-Sen University, Guangzhou 510275, P. R. China*

Yiyi Ou − *MOE Key Laboratory of Bioinorganic and Synthetic Chemistry, KLGHEI of Environment and Energy Chemistry, School of Chemistry, Sun Yat-Sen University, Guangzhou 510275, P. R. China;* orcid.org/0000-0002-2111-5064

Zeming Qi − *National Synchrotron Radiation Laboratory, University of Science and Technology of China, Hefei 230029, P. R. China*

Jianhui Zhang − *MOE Key Laboratory of Bioinorganic and Synthetic Chemistry, KLGHEI of Environment and Energy Chemistry, School of Chemistry, Sun Yat-Sen University, Guangzhou 510275, P. R. China*

Yan Huang − *Beijing Synchrotron Radiation Facility, Institute of High Energy Physics, Chinese Academy of Sciences, Beijing 100039, P. R. China*

Pieter Dorenbos − *Faculty of Applied Sciences, Delft University of Technology, 2629 JB, Delft, The Netherlands*

Complete contact information is available at:
https://pubs.acs.org/10.1021/acs.inorgchem.0c02714

Notes
The authors declare no competing financial interest.

ACKNOWLEDGMENTS

REFERENCES

(1) Blasse, G.; Grabmaier, B. C. *Luminescent Materials*; Springer: Berlin, 1994.
(2) Matsuzawa, T.; Aoki, Y.; Takeuchi, N.; Murayama, Y. A New Long Phosphorescent Phosphor with High Brightness, $SrAl_2O_4$: Eu^{2+}, Dy^{3+}. *J. Electrochem. Soc.* **1996**, *143*, 2670.
(3) Dorenbos, P. Fundamental Limitations in the Performance of Ce^{3+}-, Pr^{3+}-, and Eu^{2+}- Activated Scintillators. *IEEE Trans. Nucl. Sci.* **2010**, *57*, 1162−1167.
(4) Pust, P.; Weiler, V.; Hecht, C.; Tücks, A.; Wochnik, A. S.; Henß, A. K.; Wiechert, D.; Scheu, C.; Schmidt, P. J.; Schnick, W. Narrow-Band Red-Emitting $Sr[LiAl_3N_4]$: Eu^{2+} as a Next-Generation LED-Phosphor Material. *Nat. Mater.* **2014**, *13*, 891−896.
(5) Tang, Z.; Zhang, G.; Wang, Y. Design and Development of a Bluish-Green Luminescent Material ($K_2HfSi_3O_9$: Eu^{2+}) with Robust Thermal Stability for White Light-Emitting Diodes. *ACS Photonics* **2018**, *5*, 3801−3813.
(6) Ma, F.; Su, F.; Zhou, R.; Ou, Y.; Xie, L.; Liu, C.; Jiang, D.; Zhang, Z.; Wu, Q.; Su, L.; Liang, H. The Defect Aggregation of RE^{3+} (RE = Y, La ∼ Lu) in MF_2 (M = Ca, Sr, Ba) Fluorites. *Mater. Res. Bull.* **2020**, *125*, 110788.

(7) Shi, R.; Ning, L.; Huang, Y.; Tao, Y.; Zheng, L.; Li, Z.; Liang, H. $Li_4SrCa(SiO_4)_2$: Eu^{2+}: A Potential Temperature Sensor with Unique Optical Thermometric Properties. *ACS Appl. Mater. Interfaces* **2019**, *11*, 9691–9695.

(8) Dutta, S.; Som, S.; Meena, M. L.; Chaurasiya, R.; Chen, T. M. Multisite-Occupancy-Driven Intense Narrow-Band Blue Emission from $Sr_5SiO_4Cl_6$: Eu^{2+} Phosphor with Excellent Stability and Color Performance. *Inorg. Chem.* **2020**, *59*, 1928–1939.

(9) Liao, H.; Zhao, M.; Molokeev, S. M.; Liu, Q.; Xia, Z. Learning from a Mineral Structure toward an Ultra-Narrow-Band Blue-Emitting Silicate Phosphor $RbNa_3(Li_3SiO_4)_4$: Eu^{2+}. *Angew. Chem., Int. Ed.* **2018**, *57*, 11728–11731.

(10) Qiao, J.; Zhou, G.; Zhou, Y.; Zhang, Q.; Xia, Z. Divalent Europium-Doped Near-Infrared-Emitting Phosphor for Light-Emitting Diodes. *Nat. Commun.* **2019**, *10*, 5267.

(11) Hou, D.; Ma, C. G.; Liang, H.; Brik, M. G. Electron-Vibrational Interaction in the 5d States of Eu^{2+} Ions in $Sr_{6-x}Eu_xBP_5O_{20}$ (x = 0.01– 0.15). *ECS J. Solid State Sci. Technol.* **2014**, *3*, R39–R42.

(12) Nazarov, M.; Brik, M. G.; Spassky, D.; Tsukerblat, B. Crystal Field Splitting of 5d States and Luminescence Mechanism in $SrAl_2O_4$: Eu^{2+} Phosphor. *J. Lumin.* **2017**, *182*, 79–86.

(13) Ou, Y.; Zhou, W.; Hou, D.; Brik, M. G.; Dorenbos, P.; Huang, Y.; Liang, H. Impacts of 5d Electron Binding Energy and Electron-Phonon Coupling on Luminescence of Ce^{3+} in $Li_6Y(BO_3)_3$. *RSC Adv.* **2019**, *9*, 7908–7915.

(14) Zhang, L.; Zhang, J.; Pan, G.; Zhang, X.; Hao, Z.; Luo, Y.; Wu, H. Low-Concentration Eu^{2+}-Doped $SrAlSi_4N_7$: Ce^{3+} Yellow Phosphor for wLEDs with Improved Color-Rendering Index. *Inorg. Chem.* **2016**, *55*, 9736–9741.

(15) Ou, Y.; Zhou, W.; Liu, C.; Lin, L.; Brik, M. G.; Dorenbos, P.; Tao, Y.; Liang, H. Vacuum Referred Binding Energy Scheme, Electron-Vibrational Interaction, and Energy Transfer Dynamics in $BaMg_2Si_2O_7$: Ln (Ce^{3+}, Eu^{2+}) Phosphors. *J. Phys. Chem. C* **2018**, *122*, 2959–2967.

(16) Song, H.; Yim, D.; Roh, H.; Cho, I.; Kim, S.; Jin, Y.; Shim, H.; Kim, D.; Hong, K. $RbBaPO_4$: Eu^{2+}: A New Alternative Blue-Emitting Phosphor for UV-Based White Light-Emitting Diodes. *J. Mater. Chem. C* **2013**, *1*, 500–505.

(17) Wang, Y.; Brik, M. G.; Dorenbos, P.; Huang, Y.; Tao, Y.; Liang, H. Enhanced Green Emission of Eu^{2+} by Energy Transfer from the $^5D_3$ Level of Tb^{3+} in $NaCaPO_4$. *J. Phys. Chem. C* **2014**, *118*, 7002–7009.

(18) Chen, J.; Zhao, W.; Zhong, J.; Lan, L.; Wang, J.; Wang, N. Synthesis and Luminescence Properties of Ce^{3+}-Doped $RbBaPO_4$. *Ceram. Int.* **2014**, *40*, 15241–15248.

(19) Zhao, C.; Xia, Z.; Yu, S. Thermally Stable Luminescence and Structure Evolution of $(K, Rb)BaPO_4$: Eu^{2+} Solid-Solution Phosphors. *J. Mater. Chem. C* **2014**, *2*, 6032–6039.

(20) Zhou, R.; Lin, L.; Liu, C.; Dorenbos, P.; Tao, Y.; Huang, Y.; Liang, H. Insight into Eu Redox and Pr^{3+} 5d Emission in $KSrPO_4$ by VRBE Scheme Construction. *Dalton Trans.* **2018**, *47*, 306–313.

(21) Nair, G. B.; Swart, H.C.; Dhoble, S.J. Analysis of the Electron-Vibrational Interaction in the 5d States of Eu^{2+} Ions in $LiSrPO_4$ Host Matrix. *J. Lumin.* **2019**, *214*, 116564.

(22) Coelho, A. A. *TOPAS Academic*, Ver. 4; Coelho Software: Brisbane, Australia, 2007.

(23) Xia, Z.; Xu, Z.; Chen, M.; Liu, Q. Recent Developments in the New Inorganic Solid-State LED Phosphors. *Dalton Trans.* **2016**, *45*, 11214–11232.

(24) Ueda, J.; Dorenbos, P.; Bos, A. J. J.; Meijerink, A.; Tanabe, S. Insight into the Thermal Quenching Mechanism for $Y_3Al_5O_{12}$:Ce^{3+} through Thermoluminescence Excitation Spectroscopy. *J. Phys. Chem. C* **2015**, *119*, 25003–25008.

(25) Dorenbos, P. Relation Between Eu^{2+} and Ce^{3+} f ↔ d-Transition Energies in Inorganic Compounds. *J. Phys.: Condens. Matter* **2003**, *15*, 4797–4807.

(26) Lin, C.; Xiao, Z.; Guo, G.; Chan, T.; Liu, R. Versatile Phosphate Phosphors $ABPO_4$ in White Light-Emitting Diodes:

Collocated Characteristic Analysis and Theoretical Calculations. *J. Am. Chem. Soc.* **2010**, *132*, 3020–3028.

(27) Nair, G. B.; Bhoyar, P. D.; Dhoble, S. J. Exploration of Electron-Vibrational Interaction in the 5d States of Eu^{2+} Ions in $ABaPO_4$ (A = Li, Na, K and Rb) Phosphors. *Luminescence* **2017**, *32*, 22–29.

(28) Wang, D.; Liu, W.; Zhang, Z. Emission Tuning Studies in $BaMgSiO_4$: RE (RE = Eu^{2+}, Sr^{2+}) for White LEDs. *Mater. Chem. Phys.* **2018**, *207*, 479–488.

(29) Liu, X.; Xie, W.; Lü, Y.; Feng, J.; Tang, X.; Lin, J.; Dai, Y.; Xie, Y.; Yan, Y. Multichannel Luminescence Properties of Mixed-Valent Eu^{2+}/Eu^{3+} Coactivated $SrAl_3BO_7$ Nanocrystalline Phosphors for Near-UV LEDs. *Inorg. Chem.* **2017**, *56*, 13829–13841.

(30) Lin, L.; Shi, R.; Zhou, R.; Peng, Q.; Liu, C.; Tao, Y.; Huang, Y.; Dorenbos, P.; Liang, H. The Effect of Sr^{2+} on Luminescence of Ce^{3+}-Doped $(Ca, Sr)_2Al_2SiO_7$. *Inorg. Chem.* **2017**, *56*, 12476–12484.

(31) Nazarov, M.; Tsukerblat, B.; Noh, D. Vibronic Coupling Parameters and Stokes Shift in Thiogallate Phosphors. *J. Phys. Chem. Solids* **2008**, *69*, 2605–2612.

(32) Shannon, R. D. Revised Effective Ionic Radii and Systematic Studies of Interatomic Distances in Halides and Chalcogenides. *Acta Crystallogr., Sect. A: Cryst. Phys., Diffr., Theor. Gen. Crystallogr.* **1976**, *32*, 751–767.

(33) Wu, Z.; Fu, H.; Liu, J.; Kuang, S.; Wu, M.; Xu, J.; Kuang, X. Synthesis, Crystal Structure and Photoluminescence Properties of New Blue-Green $Ba_{1-x}(PO_3)_2$: Eu_x^{2+} $(0 < x \leq 0.040)$ Phosphors for Near Ultraviolet Based White Light-Emitting Diodes. *RSC Adv.* **2015**, *5*, 42714–42720.

(34) Qiao, J.; Ning, L.; Molokeev, M. S.; Chuang, Y.; Liu, Q.; Xia, Z. Eu^{2+} Site Preferences in the Mixed Cation $K_2BaCa(PO_4)_2$ and Thermally Stable Luminescence. *J. Am. Chem. Soc.* **2018**, *140*, 9730–9736.

(35) Zhou, R.; Liu, C.; Lin, L.; Huang, Y.; Liang, H. Multi-Site Occupancies of Eu^{2+} in $Ca_6BaP_4O_{17}$ and Their Potential Optical Thermometric Applications. *Chem. Eng. J.* **2019**, *369*, 376–385.

(36) Martín, I. R.; Rodríguez, V. D.; Rodríguez-Mendoza, U. R.; Lavín, V.; Montoya, E.; Jaque, D. Energy Transfer with Migration. Generalization of the Yokota-Tanimoto Model for Any Kind of Multipole Interaction. *J. Chem. Phys.* **1999**, *111*, 1191–1194.

(37) Georgescu, S.; Voiculescu, A. M.; Matei, C.; Stefan, A.; Toma, O.; Birjega, R. Upconversion Luminescence in Langatate Ceramics Doped with Tm^{3+} and Yb^{3+}. *J. Lumin.* **2014**, *154*, 74–79.

(38) Liu, C.; Qi, Z.; Ma, C.; Dorenbos, P.; Hou, D.; Zhang, S.; Kuang, X.; Zhang, J.; Liang, H. High Light Yield of $Sr_8(Si_4O_{12})Cl_8$: Eu^{2+} under X-ray Excitation and Its Temperature-Dependent Luminescence Characteristics. *Chem. Mater.* **2014**, *26*, 3709–3715.